

This paper was recommended for publication in revised form by Regional Editor Derya Burcu Özkan

AERODYNAMIC PERFORMANCE OF SMALL-SCALE HORIZONTAL AXIS WIND TURBINES UNDER TWO DIFFERENT EXTREME WIND CONDITIONS

***Emre ALPMAN**

Marmara University Mechanical Engineering Department
Istanbul, Turkey

Keywords: Horizontal axis wind turbines, extreme wind conditions, computational fluid dynamics

** Corresponding author, Phone: +90 216 348 02 92 / 546, Fax: +90 216 348 02 93*

E-mail address: emre.alpman@marmara.edu.tr

ABSTRACT

Aerodynamic performance of two small-scale horizontal axis wind turbines are analyzed under the extreme operating gust and extreme direction change conditions with initial wind speeds of 7, 10, 13, 15 and 20 m/s. Performance predictions are performed using computational fluid dynamics, and time variations of shaft torque and hub bending moment produced by the turbines are presented and compared with each other. Sectional flow field and sectional blade loading details along with surface skin friction line predictions are also presented in order to explain the loading behavior of the turbine blades at the mentioned extreme wind conditions. Predictions show that variations in wind speed and blade loadings are similar at low wind speeds, however, this similarity degrades as the wind speed increases. Also compared to wind speed changes, aerodynamic forces are shown to adapt more slowly to wind direction changes.

INTRODUCTION

Wind turbine blades are aerodynamically designed by searching for suitable design parameters that maximize the energy production at low cost [1]. The annual energy production of turbine at a given wind site should be calculated for this purpose. This calculation is done by multiplying the power produced at a given wind speed with the probability of occurrence of that wind speed in a year, and then integrating this product between cut-in and cut-out speeds of the turbine [2]. Typically, steady state or time averaged power values produced at corresponding wind speeds are used in annual energy production calculations [3] -[9]. However, it is well-known that a wind turbine spends majority of its life at unsteady wind conditions [10]. Time dependent wind

conditions were shown to significantly affect the performance of a wind turbine [11]. International Standard IEC 61400-1 outlines the minimum design requirements for horizontal axis wind turbines (HAWT) [12]. According to this standard, performance of a turbine and loading on its blades at extreme wind conditions is one of the elements that must be considered in order to ensure proper safety and reliability. Two of the extreme wind conditions specified in this standard are the extreme operating gust (EOG) where wind speed experiences transient oscillations and the extreme direction change (EDC) where the yaw error gradually increases from zero to a positive value.

Wind turbine performance under unsteady wind conditions has been analyzed in the literature using various techniques. Storey et al. simulated turbine loads during extreme coherent gust [13]. Here, the flow field was simulated using computational fluid dynamics with Large Eddy Simulation for turbulence and the effect of the turbines were introduced using an actuator sector model [14]. Jeong et al. investigated the effect of wake on the aeroelastic behavior of a HAWT under sheared turbulent flow [15]. The predictions were performed for normal wind profile and extreme wind shear conditions [12] using blade element momentum theory and free wake method. Kim et al. performed a comparison study for a two-bladed HAWT during normal and extreme gust conditions [16] using the aeroelastic code HAWC2 [17]. This code uses an extended blade element momentum theory for aerodynamic calculations. Extensions to the blade element momentum theory were introduced to handle unsteady phenomena like dynamic inflow, dynamic stall, etc. Qui et al. [18] remark the deficiency of blade element momentum theory in simulating complex flows and simulate unsteady aerodynamics of HAWTs in yawing and

pitching conditions using a nonlinear lifting line method for blade aerodynamics along with a free vortex method for the wake. Their simulations showed that changes in yaw angle affected the shaft torque considerably. Sezer-Uzol and Uzol [19] analyzed the effect of steady and transient shear on the wake structure and performance of a two bladed HAWT rotor using vortex-lattice method. This method was also used by Jeon et al. [20] for unsteady aerodynamics prediction of an off-shore floating wind turbine in planform pitching motion. They included the thickness and viscous effects to their predictions using a nonlinear vortex correction method.

References [21] and [22] include unsteady aerodynamics simulations performed for vertical axis wind turbines (VAWT). In these references performance of straight bladed Darrieus type turbines under fluctuating wind conditions were analyzed by solving the unsteady Reynolds Averaged Navier Stokes (URANS) equations around the blades. In both studies flow around the straight blades was assumed to be two-dimensional.

This study includes performance predictions of two different two-bladed HAWT rotors under the EOG and EDC conditions. Here, flow field simulations are performed by solving URANS equations in a flow domain surrounding both blades of the rotors. This way; viscous, turbulence and three-dimensional effects are all included in to the predictions. The first turbine studied is the NREL Phase VI horizontal axis experimental wind turbine [7]. It is a stall regulated turbine with a rated power of 20 kW and rotor diameter of 10.06 m. The second turbine has the same rated power and diameter with those of NREL Phase VI but its blades were aerodynamically optimized for maximum annual energy production using genetic algorithm [6]. Blade parameters for optimizations were chord length and twist angle distributions along the blade span, the pitch angle of the blades and airfoil profiles for the root, primary and tip portions of the blades [5], [6]. In Ref. [6] chord length and twist angle distributions along the blade span were defined using cubic Bezier curves with different number of control points. In this study, the design obtained using three control points, which yielded the best annual energy production value in [6], will be used.

The analyses are performed at initial wind speeds of 7, 10, 13, 15 and 20 m/s. Here, the effect of wind shear was neglected and oncoming wind distribution was assumed to be uniform. In the extreme operating gust condition wind velocity remains perpendicular to the rotor disc but its magnitude changes, while in the extreme direction change case, the magnitude of the wind speed remains constant but its direction changes. Unsteady shaft torque, bending moment and power coefficient predictions are presented for simulations of 15 seconds of real time for both wind conditions.

Section 2 contains the methodology followed during this study while the results obtained are presented and discussed in section 3. Finally, conclusions are drawn in section 4.

NOMENCLATURE

D	Rotor diameter
I_{ref}	Expected value of turbulence intensity at 15 m/s

$V(z, t)$	Wind Speed as a function of elevation and time
$V(z)$	Normal wind profile
V_{ave}	Average wind velocity
V_{e1}	Extreme wind speed with a recurrence of one year
V_{gust}	Hub height gust magnitude
V_{hub}	Wind speed at hub location
V_{ref}	Reference wind velocity
t	Time
T	Gust or direction change period
z	Elevation
z_{hub}	Hub elevation
$\theta(t)$	Yaw angle
θ_e	Magnitude of the direction change
σ_1	Turbulence standard deviation
Λ_1	Longitudinal turbulence scale parameter at hub height

METHODOLOGY

Flow field predictions were obtained using computational fluid dynamics (CFD). FINE-TURBO package of NUMECA software [23] was used to solve URANS equations around the turbine blades. For numerical solutions a block structured mesh consisting of nearly 4.2 million points was constructed using AutoGrid5 package of NUMECA [23]. In order to use the same mesh for both of the extreme wind speed cases, the mesh was constructed for the full geometry (around both blades) in order to account for non-symmetry that would occur for the EDC case. The inflow boundary of the flow domain was located at five blade radii upstream of the rotor while the outflow boundary was located at ten blade radii downstream. The external boundary was five blade radii away from center of rotation. No-slip adiabatic wall conditions were imposed on the solid boundaries along with a wall model for turbulence [23]. Spalart-Allmaras one equation turbulence model was used during the computations [24]. Wind speed, air density and molecular viscosity were specified at the inflow boundary. The relevant values were obtained from [25]. Inflow conditions for turbulent eddy viscosity was specified according to the guidelines specified at [26] for external flows. Pressure was specified at the outflow boundary and farfield boundary conditions were applied at the external boundaries. The resulting surface mesh around one of the NREL Phase VI blades can be seen in Figure 1.

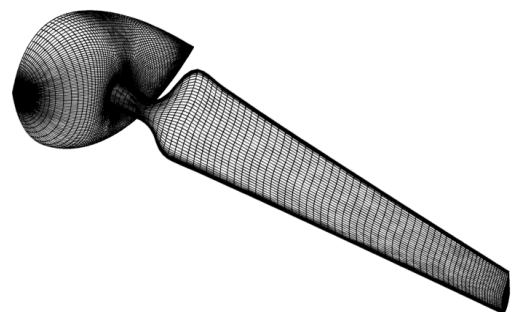


Figure 1. Surface mesh on one NREL Phase VI blade

In the extreme operating gust model as given in IEC 61400-1 standard [12], the wind speed is defined as

$$V(z, t) = \begin{cases} V(z) - 0.37V_{gust} \sin\left(\frac{3\pi t}{T}\right) \left(1 - \cos\left(\frac{2\pi t}{T}\right)\right) & \text{for } 0 \leq t \leq T \\ V(z) & \text{otherwise} \end{cases} \quad (1)$$

where $V(z)$ is called the normal wind profile [12] and it defines the vertical wind shear across the rotor. However, since wind shear effects were neglected in this study, $V(z)$ was taken to be constant and equal to the initial wind speed at the hub. The T appearing in equation (1) was taken 10.5 seconds as suggested in [12]. V_{gust} is the hub height gust magnitude [12] and is defined as

$$V_{gust} = \min\left(1.35(V_{e1} - V_{hub}), 3.3\left(\frac{\sigma_1}{1+0.1\left(\frac{D}{\Lambda_1}\right)}\right)\right) \quad (2)$$

where D is rotor diameter, V_{hub} is the wind speed at hub location and σ_1 is the turbulence standard deviation [12];

$$\sigma_1 = I_{ref}(0.75 V_{hub} + b) \quad (3)$$

In equation (3) $b = 5.6$ m/s and I_{ref} is the expected value of turbulence intensity at 15 m/s [12]. From Table 1 of [12] I_{ref} was taken as 0.16. The longitudinal turbulence scale parameter Λ_1 at hub height z is calculated using [12]

$$\Lambda_1 = \begin{cases} 0.7z & z \leq 60 \text{ m} \\ 42 \text{ m} & z > 60 \text{ m} \end{cases} \quad (4)$$

Extreme wind speed with a recurrence of one year, V_{e1} , is defined as [12]

$$V_{e1} = 1.12V_{ref}\left(\frac{z}{z_{hub}}\right)^{0.11} \quad (5)$$

where reference velocity V_{ref} is related to the average wind velocity V_{ave} according to [12]

$$V_{ave} = 0.2 V_{ref} \quad (6)$$

Since wind shear effects were neglected in this study, the term z/z_{hub} in equation (5) was taken as 1.

In the extreme direction change model as given in IEC 61400-1 standard [12], the magnitude of the direction change, which is limited to $\pm 180^\circ$ interval, is given by:

$$\theta_e = \pm \tan^{-1}\left(\frac{\sigma_1}{V_{hub}\left(1+0.1\left(\frac{D}{\Lambda_1}\right)\right)}\right) \quad (7)$$

Then, the direction change transient is calculated using

$$\theta(t) = \begin{cases} 0^\circ & \text{for } t < 0 \\ \pm\theta_e \left(1 - \cos\left(\frac{\pi t}{T}\right)\right) & \text{for } 0 \leq t \leq T \\ \theta_e & \text{for } t > T \end{cases} \quad (8)$$

Here, the duration of the direction change, T , is taken as 6 seconds as suggested in [12]. The sign in equations (7) and (8) is chosen such that the worst transient loading is observed [12]. In this study, this direction is selected to be positive.

RESULTS AND DISCUSSION

Flow field predictions for the NREL Phase VI rotor and the aerodynamically optimized rotor from reference [6] were obtained for EOG and EDC conditions. Numerical solutions were performed for initial wind speeds of 7, 10, 13, 15 and 20

m/s. During the computations, rotor blades of both turbines were assumed to rotate at a constant angular speed of 72 rpm.

The performance of the turbines at steady wind conditions are compared in Figure 2, which displays shaft torque predictions for the turbines at steady wind speeds of 7, 10, 13 and 15 m/s. Experimental data for the NREL Phase VI rotor [27] were also included to the figure in order to test the accuracy of the predictions. The figure showed that numerical solutions for the NREL Phase VI rotor were in good agreement with measurements at 7 and 15 m/s wind speeds, however, the shaft torque was clearly over-predicted at the other wind speeds. Similar differences between predictions in measurements were also observed in previous studies [5], [25], [27]. Figure 2 also showed that the optimized blade produces a slightly higher torque at low wind speeds while NREL Phase VI turbine displays a better performance at 13 m/s wind speed. The power values produced by the turbines at 15 m/s are nearly same. Aerodynamic performances of the turbines are similar because during the optimization studies performed in reference [6], the rated power of the optimized turbine was not allowed to exceed 110% of the rated power of NREL Phase VI turbine. The optimized rotor produces a slightly higher torque at low wind speeds because it was optimized for Gökçeada, Turkey location where mean and most probable wind speeds are 8.8 m/s and 6 m/s, respectively.

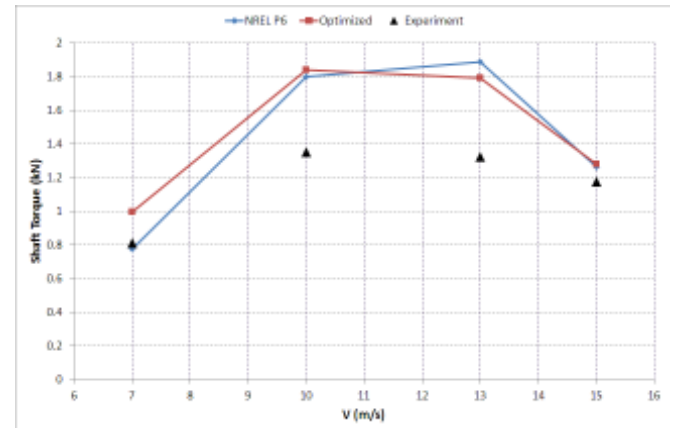


Figure 2. Shaft torque predictions at steady wind speeds

Extreme Operating Gust

Figure 3 displays shaft torque and hub bending moment predictions for the blades for initial wind speed of 7 m/s. Unsteady wind speed profile is also added to the figure for comparison. It is clear from this figure that the torque and bending moment variations are similar in shape with the wind speed variation. However, there is a slight lag in the torque variation due to the inertia of air. The optimized rotor produces

slightly higher torque than the NREL Phase VI rotor however; its blades are subjected to considerably higher bending moments. In [6], the blades were optimized for maximum

annual energy production; however, no constraint was introduced to limit the thrust force or the bending moment developing on the blades.

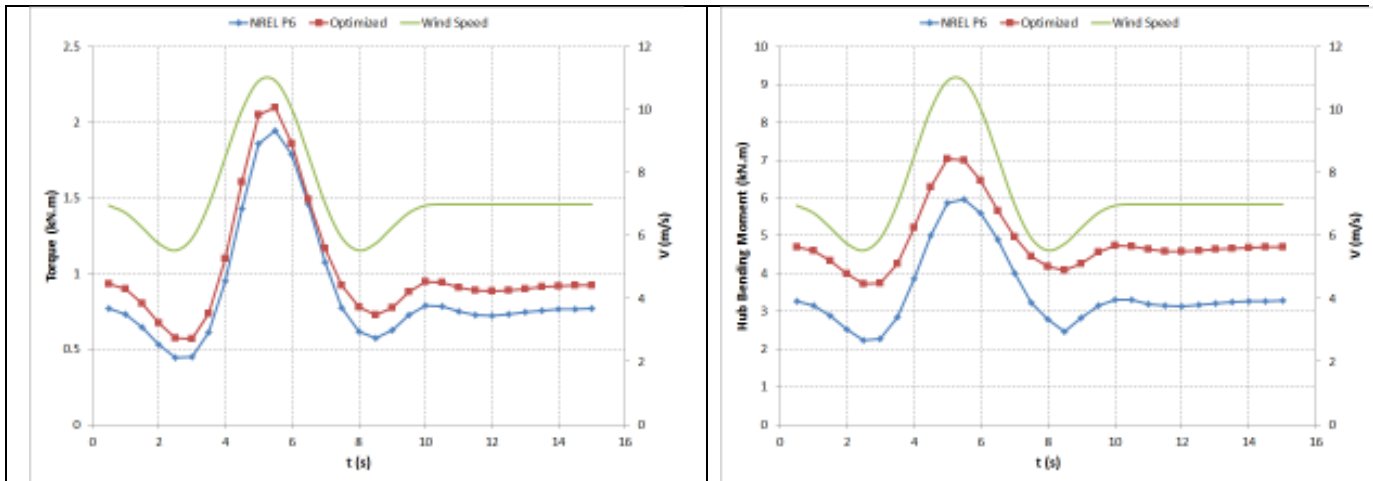


Figure 3. Variation of rotor torque (left) and hub bending moment (right) with time (EOG, $V_0 = 7$ m/s)

In order to compare the flow fields over the blades of the turbines, skin friction lines on the suction sides of the NREL Phase VI (left column) and optimized (right column) rotor blades at $t = 5, 5.5, 6, 6.5$ seconds are displayed in Figure 4. Here, time increases from top to bottom. Converging of skin

friction lines as shown in the figure indicates flow separation. It is clear that the separated region on the optimized blade is larger than that on NREL Phase VI blade. This explains the higher bending moment the optimized blade experiences.

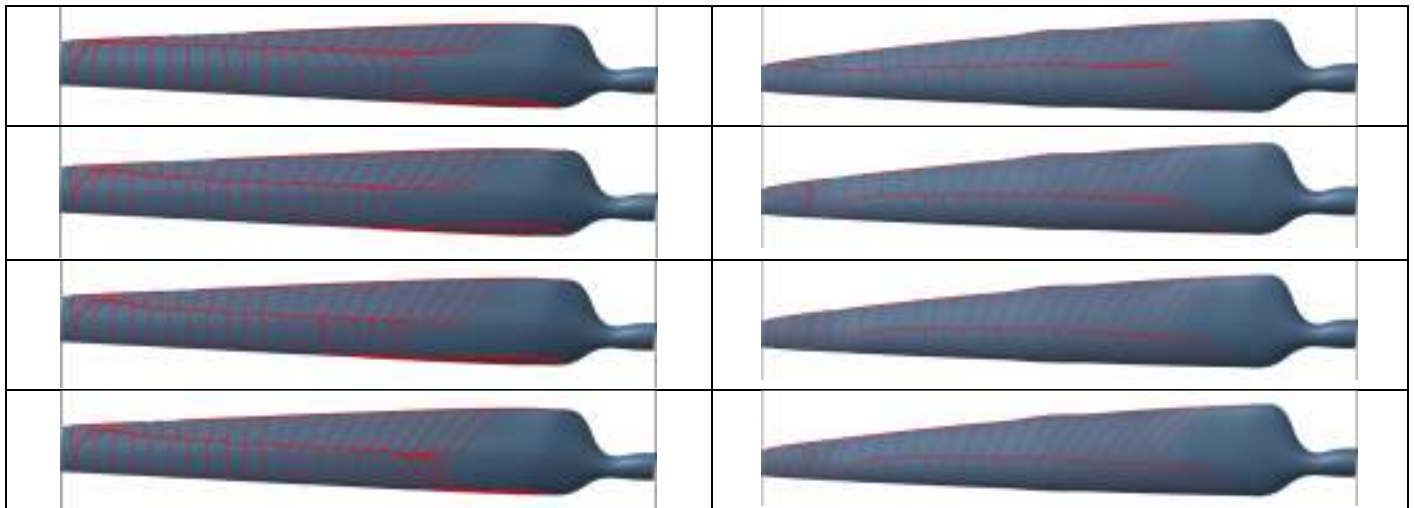


Figure 4. Skin friction lines on the suction side of NREL Phase VI (left), and optimized (right) rotor blade at $t = 5, 5.5, 6, 6.5$ seconds.

Variation of power coefficients of the turbines in time are shown in Figure 5. Here, the power coefficient is calculated using the instantaneous wind speed. Although the predicted torque variations were similar to wind speed variation, predicted power coefficients shows an almost opposite behavior. This indicates that the aerodynamic forces did not develop as fast as the wind speed changed. One interesting

consequence of this can be observed at about the 8th second where the wind speed reaches its minimum. Here, the power coefficient of the rotor temporarily exceeds 0.7 which is well above the Betz limit [1].

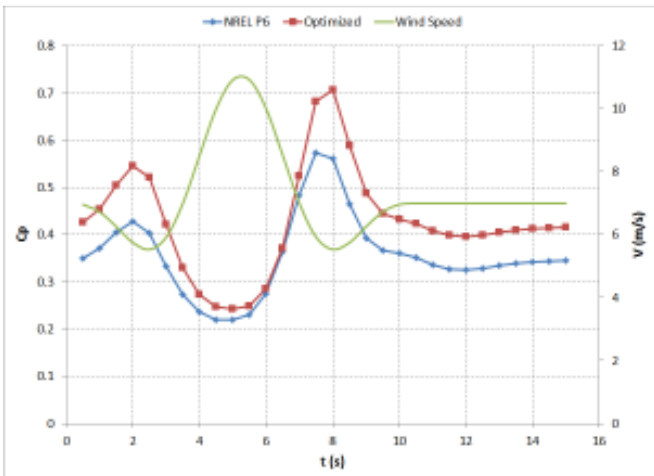


Figure 5. Variation of power coefficient with time ($V_0 = 7$ m/s)

Shaft torque and hub bending moment predictions for the blades for the initial wind speed of 10 m/s are displayed in Figure 6. Unlike the predictions for the 7 m/s initial wind speed, both torque and bending moment reach their maximum values before the wind speed does. Here, the optimized blade reaches its peak earlier than NREL Phase VI blade. In addition to this, torque and bending moment predictions for the NREL Phase VI rotor showed a faster increase between 3rd and the 5th seconds compared to the predictions for the optimized rotor.

Figure 7 displays the skin friction lines on the suction sides of the blades plotted at $t = 4, 4.5, 5, 5.5$ and 6 seconds. A close examination of these lines reveals that; the flow remains attached around the leading edge of the NREL Phase VI blade, especially at the outboard stations where the moment arm is

long. On the other hand, flow over the outboard stations of the optimized blade is fully separated and there is a much smaller region of attached flow around the leading edge at the mid sections. Larger attached flow region on the suction side of the NREL Phase VI turbine leads to a faster increase of its torque output compared to that of the optimized rotor. However, unexpectedly, the bending moment on NREL Phase VI rotor also increases faster than and exceeds the bending moment of the optimized rotor between 3rd and the 5th seconds. In order to investigate this, sectional bending moments (per unit spanwise length) at the 5th second on different spanwise stations of the blades are displayed in Figure 8. Here at 35% and 75% radius stations, sectional bending moment on the NREL Phase VI blade is slightly higher than that of the optimized blade. However, this difference considerably increases at the 95% radius station. This is mainly due to the airfoil sections used at this outboard station. The NREL Phase VI blade has S809 airfoil profile [28] at all spanwise locations [7]. However, the optimized blade has E387 airfoil profile [29] at the tip section ($> 90\%$ radius) [5], [6]. S809 is 21% thick airfoil and it is recommended as a “primary” airfoil for small wind turbines [30]. Inspecting the table shown in [30], one can conclude that thinner airfoils are more suitable for tip regions of wind turbine blades. Being only 9.1% thick, E387 is originally designed for sail planes [31] it has good drag characteristics at moderate and high Reynolds numbers [31]. It is mainly this characteristic of the E387 airfoil that kept the bending moment of the optimized rotor below that of NREL Phase VI as the wind speed increased.

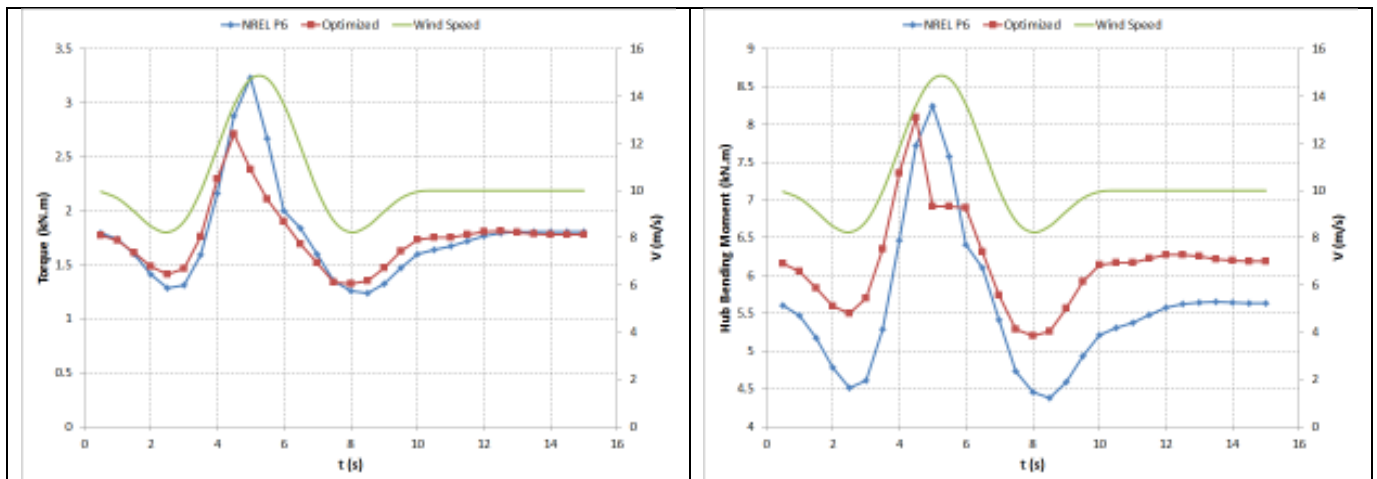


Figure 6. Variation of rotor torque (left) and hub bending moment (right) with time ($V_0 = 10$ m/s)

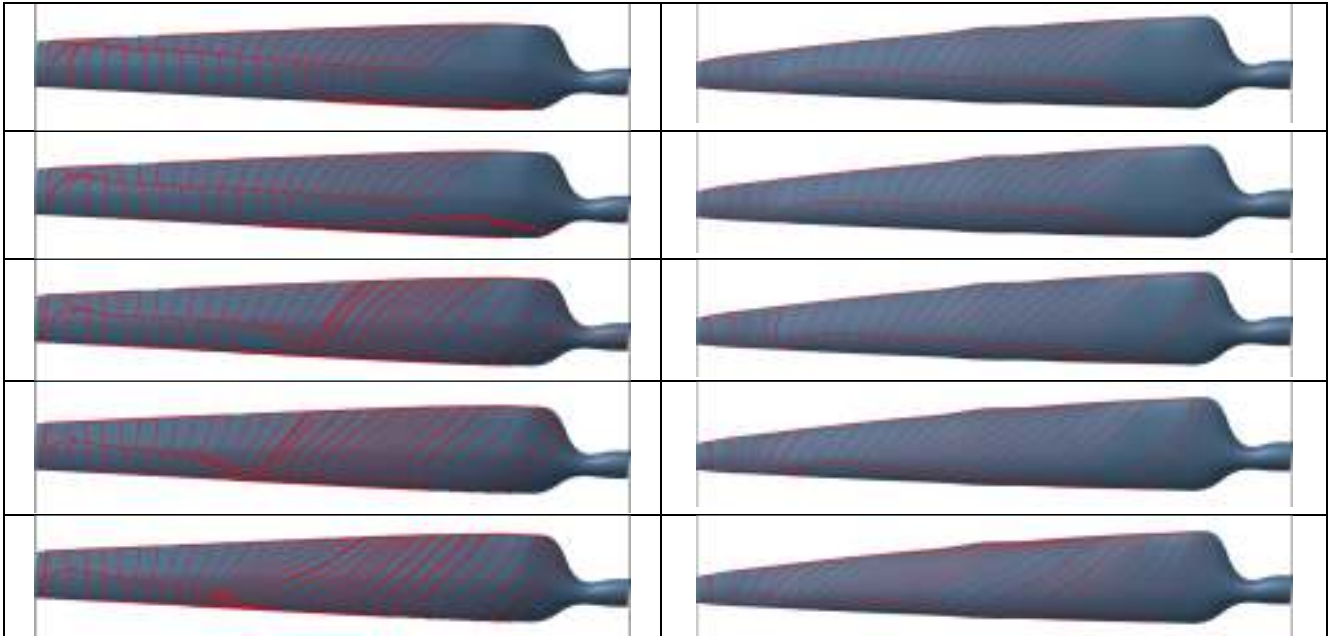


Figure 7. Skin friction lines on the suction side of NREL Phase VI (left), and optimized (right) rotor blade at $t = 4, 4.5, 5, 5.5, 6$ seconds.

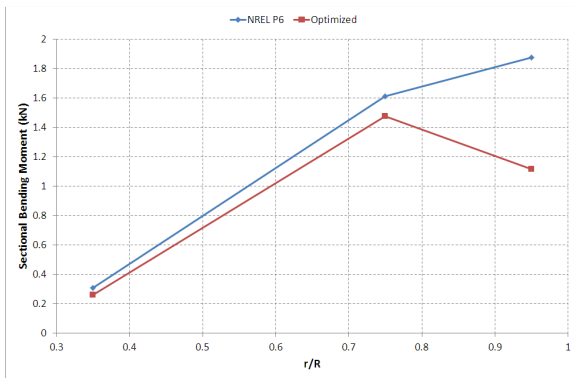


Figure 8. Sectional bending moment at different spanwise stations ($V_0 = 10$ m/s)

Shaft torque and hub bending moment predictions for the blades for initial wind speed of 13 m/s are displayed in Figure 9. In general, predictions showed a similar behavior to those obtained for 10 m/s initial wind speed. However, the decrease in the torque and the bending moment at about 8th second is greater than the corresponding drops around the 2.5th second. These are the times at which the wind speed reaches its minimum value.

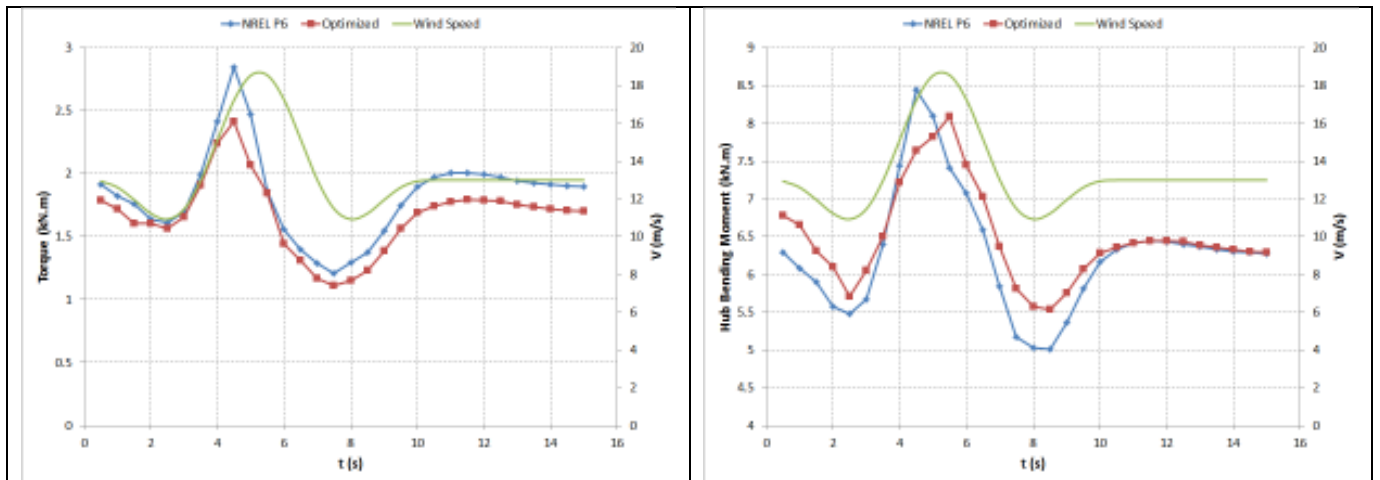


Figure 9. Variation of rotor torque (left) and hub bending moment (right) with time ($V_0 = 13$ m/s)

When the torque and bending moment predictions for 15 m/s initial wind speed are investigated from Figure 10, a very different behavior is observed for the NREL Phase VI turbine. Unlike the previous cases, torque and bending moment variations for this turbine are highly irregular, show huge spikes and look nothing like the gust profile. Even a negative torque value was predicted at about 7th second of the simulation. Torque and bending moment predictions for the optimized rotor, on the other hand, display a smooth variation in contrast to the NREL Phase VI rotor, although both turbines operate at separated flow conditions at this wind speed case. In order to understand the main reason for this huge behavior difference, contours of relative velocity magnitude around the

blade sections at 75% radius are plotted in Figure 11. The snapshots shown in this figure are taken at $t = 1.5, 2, 2.5, 3, 3.5$ and 4 seconds. Here NREL Phase VI and optimized rotor predictions are displayed on the left and the right columns of this figure, respectively. It is evident from Figure 11 that the wake of the NREL Phase VI blade section show time dependent variations, which is an indication of periodic vortex shedding and causes the highly irregular loading behavior observed in Figure 10. On the other hand, the wake of the optimized blade section varies slowly in time; hence a smooth loading behavior is observed.

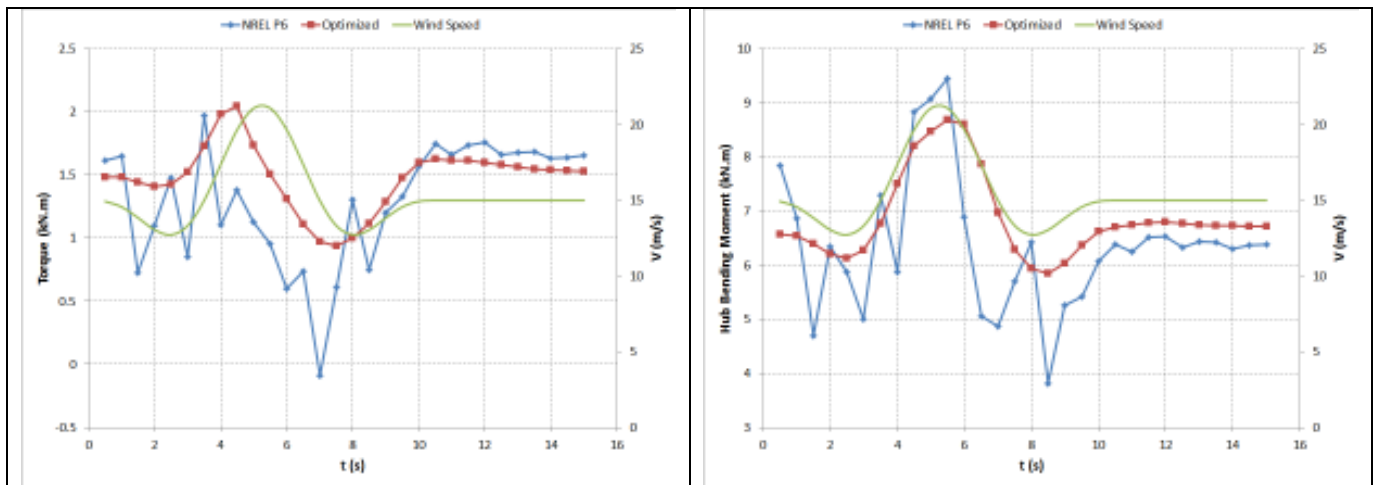


Figure 10. Variation of rotor torque (left) and hub bending moment (right) with time ($V_0 = 15$ m/s)

Figure 12 displays the shaft torque and hub bending moment predictions at initial wind speed of 20 m/s. Similar to the 15 m/s case, torque and bending moment predictions for the optimized rotor show a smooth variation in contrast to the NREL Phase VI rotor. Also, loading on the NREL Phase VI blades reaches a steady state more than two seconds later compared to the loading on the optimized blades.

Extreme Direction Change

Shaft torque and bending moment distributions for extreme direction change at a uniform wind speed of 7 m/s are displayed in Figure 13. Unsteady yaw angle profile is also added to the figure for comparison. As expected [1], the shaft torque gradually decreases as yaw angle increases. After the yaw angle becomes fixed at the 6th second, the variation in shaft torque slows down but steady state is not reached until after 14th second of the simulation. Hub bending moment predictions also

show a similar behavior to that of shaft torque. At steady yaw conditions, increasing yaw angle decreases thrust coefficient [1], and consequently the hub bending moment. At 7 m/s of wind speed the optimized rotor was shown to produce slightly higher shaft torque at the expense of higher bending moment and this is also evident from Figure 13.

In order to analyze the efficiency of the rotors, time variation of power coefficient is plotted in Figure 14. Here, power coefficient is calculated using instantaneous wind speed component normal to the rotor disk. Similar to the EOG condition, aerodynamic forces here does not develop as fast as the wind direction changes and consequently, the efficiency of the rotor temporarily increases during the wind direction change period. The optimized rotor’s power coefficient temporarily exceeding the Betz limit at the 5.5th second of the simulation is also because of this phenomenon.

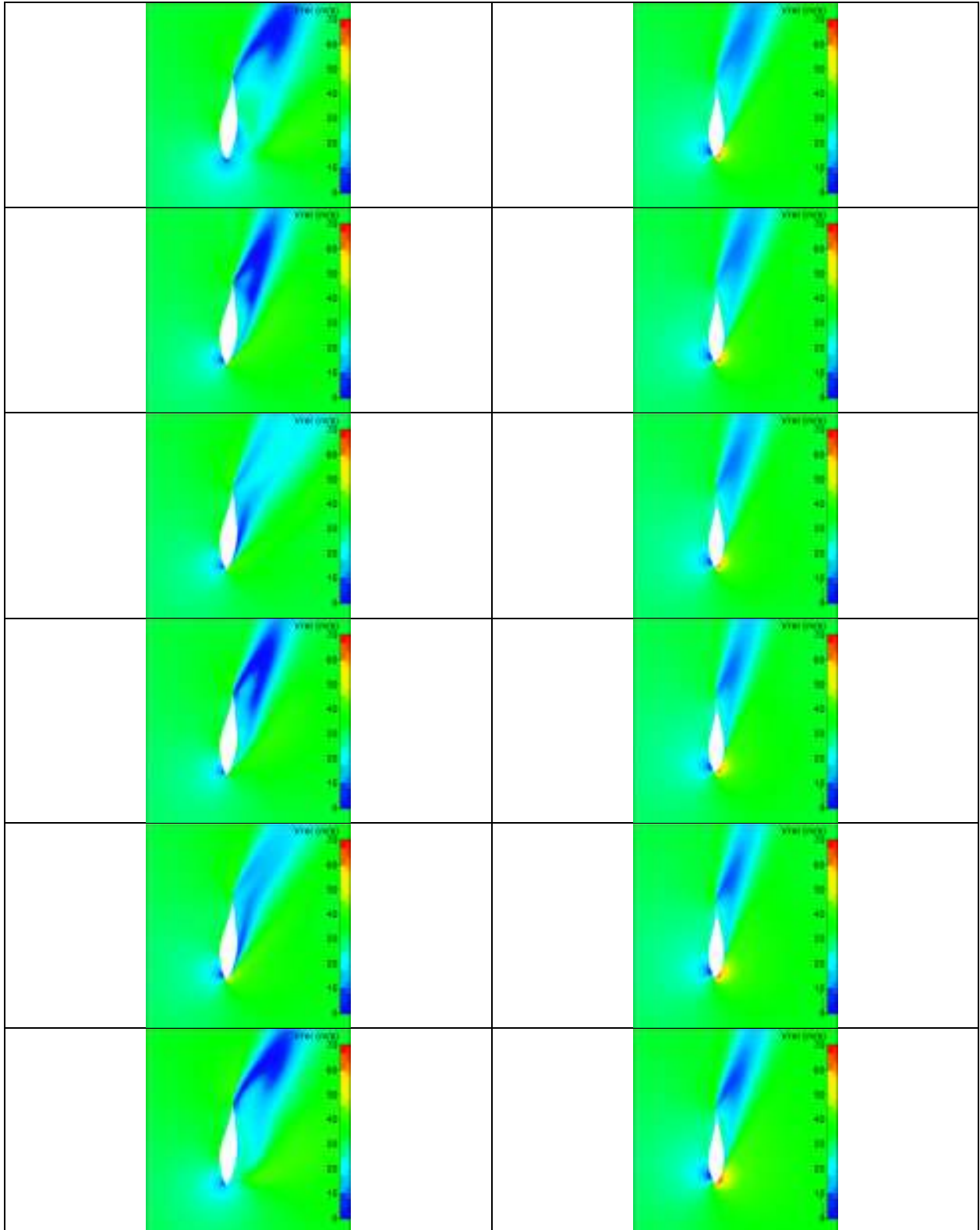


Figure 11. Contours of relative velocity magnitude at 75% radius for NREL Phase VI (left) and optimized (right) turbines at $t = 1.5, 2, 2.5, 3, 3.5$ and 4 seconds.

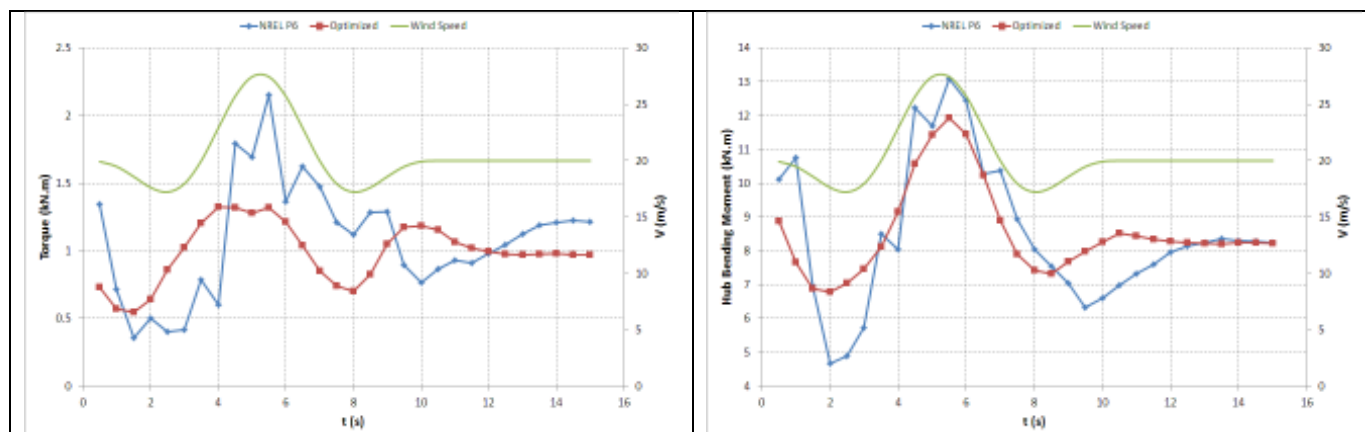


Figure 12. Variation of rotor torque (left) and hub bending moment (right) with time ($V_0 = 20$ m/s)

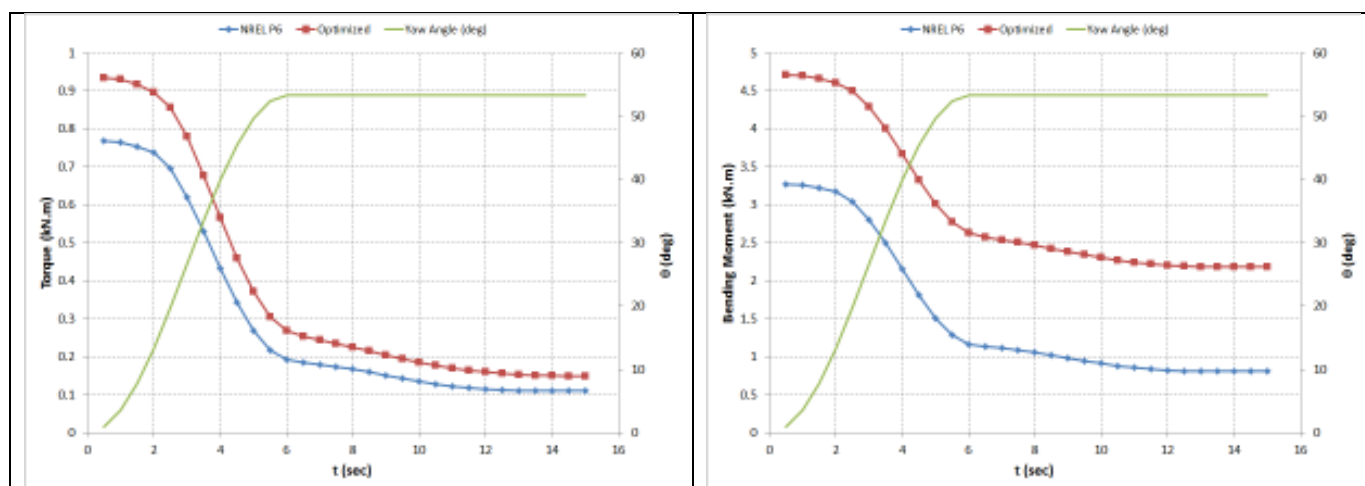


Figure 13. Variation of rotor torque (left) and hub bending moment (right) with time ($V = 7$ m/s)

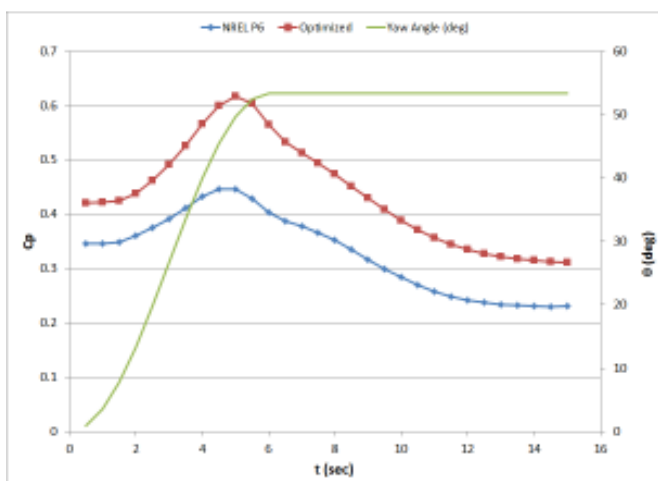


Figure 14. Variation of power coefficient with time ($V = 7$ m/s)

behavior observed for 7 m/s wind speed, both shaft torque and hub bending moment gradually decreases with increasing yaw angle. However, the amount of decrease for the NREL Phase VI rotor was predicted to be more than the optimized rotor. Also, for this wind speed the steady state is reached faster than the 7 m/s wind speed case, however, one should also note that the final yaw angle also decreased when the wind speed is increased from 7 m/s to 10 m/s.

Figure 16 displays the torque and bending moment predictions for wind speed of 13 m/s. As it was observed in the previous cases, both loadings gradually decrease as yaw angle increases. However, undershoots in the loadings were observed towards the end of the direction change period. This was in contrast to what was observed for the previous lower speed cases. In addition to this, despite the higher initial torque output of the NREL Phase VI rotor than the optimized rotor, the latter's output exceeds the formers once steady state is reached.

Shaft torque and hub bending moment predictions for 10 m/s wind speed are displayed in Figure 15. Similar to the

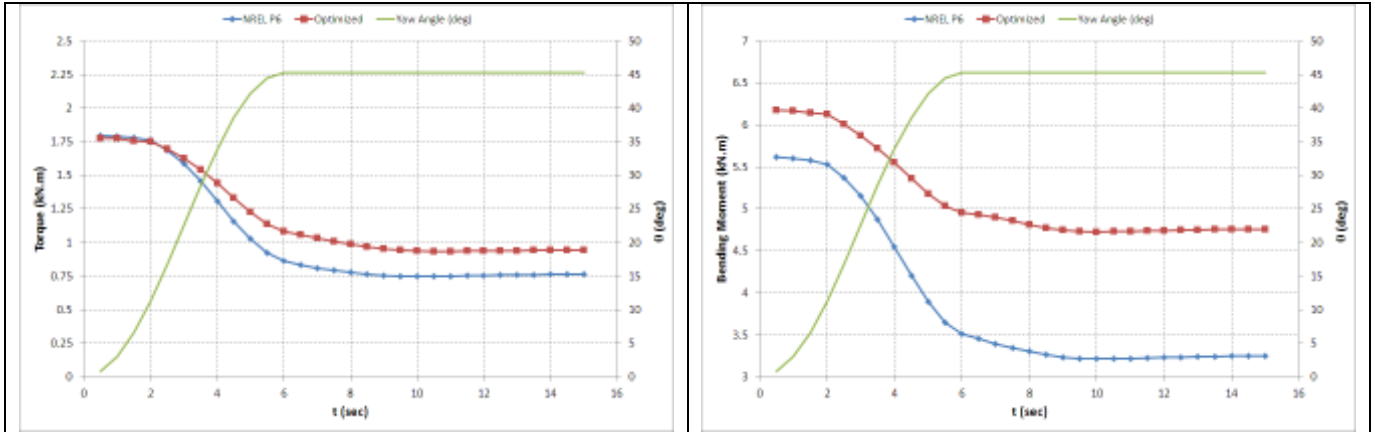


Figure 15. Variation of rotor torque (left) and hub bending moment (right) with time ($V = 10$ m/s)

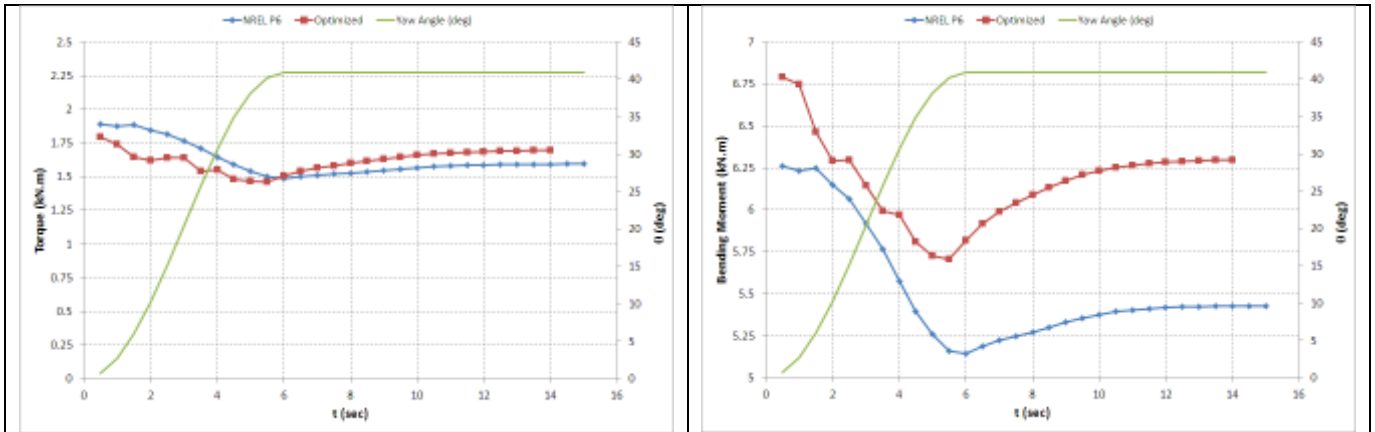


Figure 16. Variation of rotor torque (left) and hub bending moment (right) with time ($V = 13$ m/s)

Torque and bending moment predictions at 15m/s of wind speed are displayed in Figure 17. Similar to what was previously observed for the EOG condition with initial speed of 15 m/s, NREL Phase VI rotor again yields highly irregular and oscillatory loading predictions at the initial phases of the direction change. This is in contrast to smooth torque and bending moment output of the optimized rotor. However, the amplitude of the oscillations gradually decreases with time and disappears once steady state is reached. Moreover, the final torque output of both rotors is higher than their initial values even though there is more than 40 degrees of yaw error. Increasing yaw angle decreases the component of velocity normal to the rotor disk. Therefore, the amount of air crossing the rotor disk, and consequently the power available in the wind

decreases. This explains the decrease in the loadings observed for the previous lower wind speeds. However, a decrease in the velocity component normal to the disk also decreases the effective angle of attack of the blade sections and consequently diminishes the separated flow region on the suction side of the blades. In order to visualize this, the skin friction lines plotted on the suction side of the NREL Phase VI blades at the 4th, 5th, 6th, 7th and 8th seconds of the simulation are shown in Figure 18. The figure clearly shows that, initially the flow over the suction sides of the blades is almost fully separated except at the leading edge region close to the tip. However, separation line moves downstream with time and consequently the size of the attached flow region grows. This, not only increases the torque output, but also decreases the bending loading.

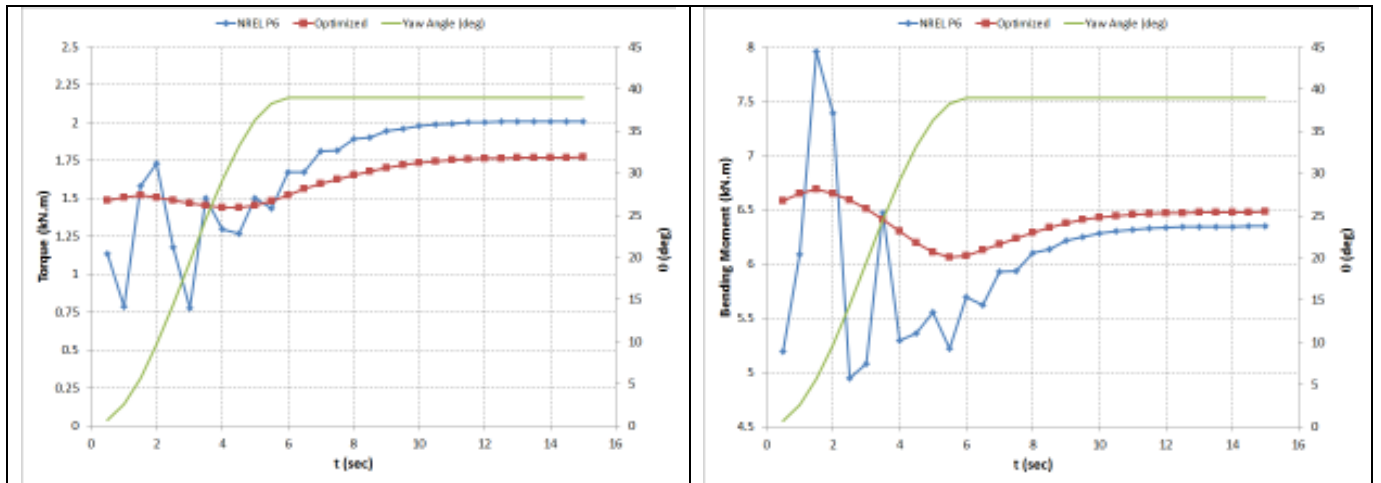


Figure 17. Variation of rotor torque (left) and hub bending moment (right) with time ($V = 15$ m/s)

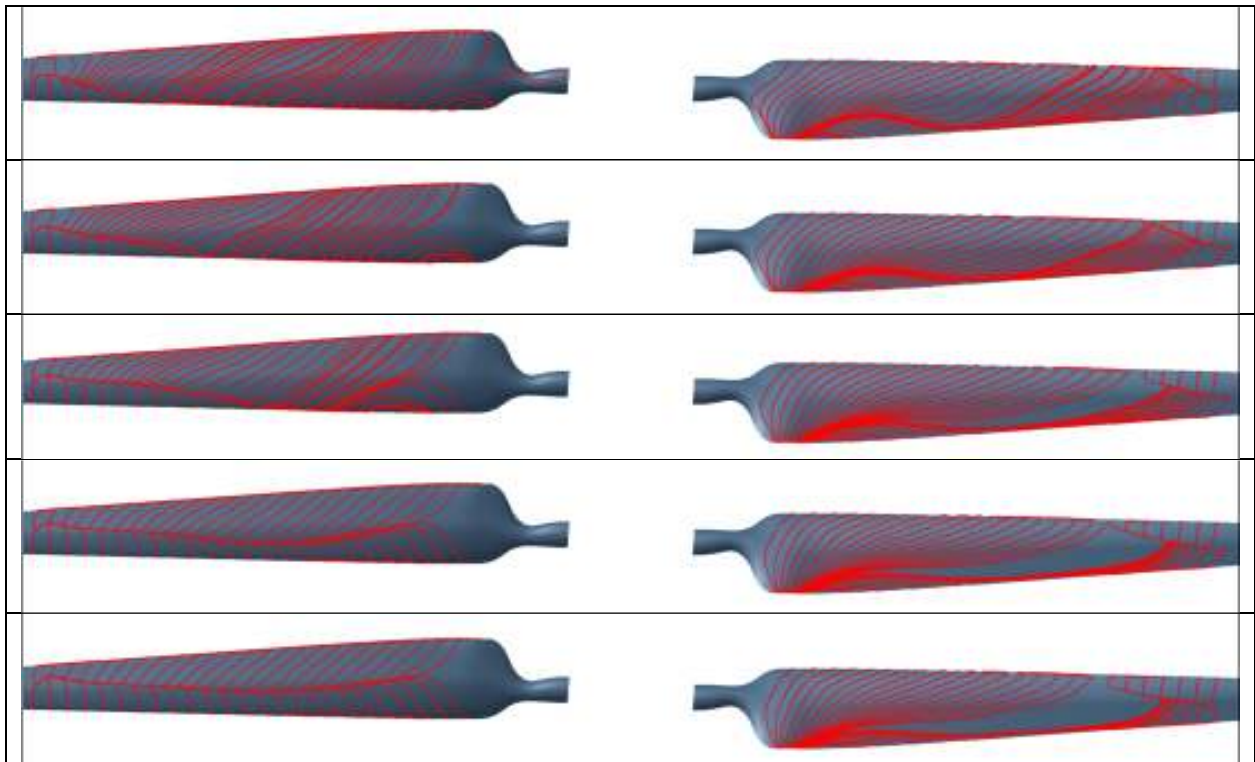


Figure 18. Skin friction lines on the suction side of NREL Phase VI blades at $t = 4, 5, 6, 7$ and 8 seconds

Finally loading predictions for 20 m/s wind speed are displayed in Figure 19. Here, torque and bending moment outputs of both turbines show oscillatory behavior at all times during the simulation. Again the amplitude of the oscillations decrease with time however, a steady condition is never reached because

the flow remains separated on the suction sides of the blades at this wind speed. At the same time, the effect of decreasing angle of attack of the blades can again be seen by considering the initial and final values of the torque and bending moment predictions.

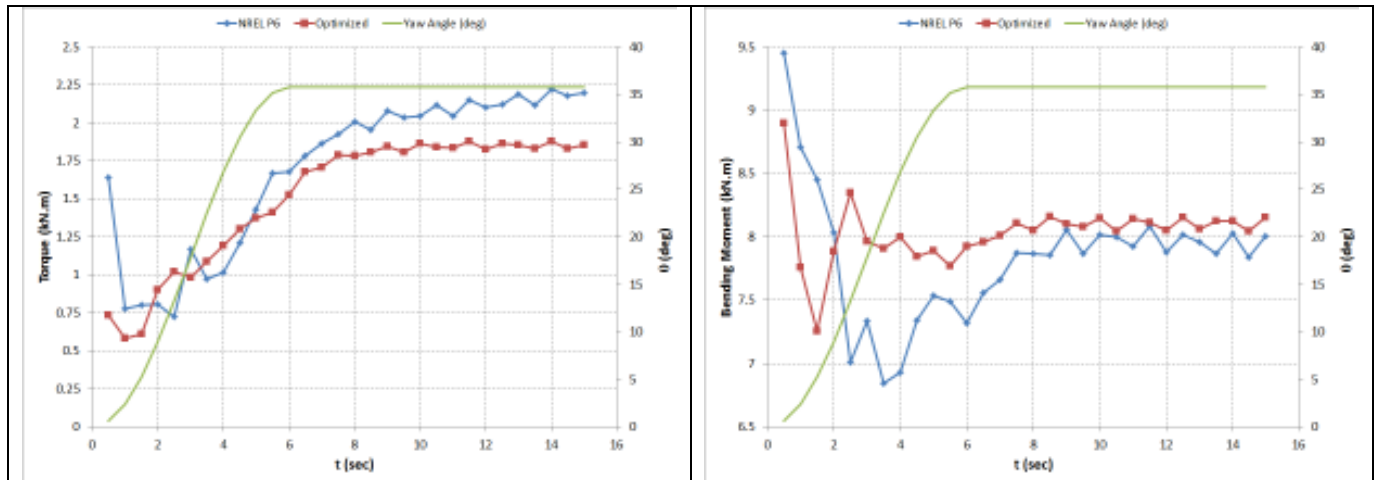


Figure 19. Variation of rotor torque (left) and hub bending moment (right) with time ($V = 20$ m/s)

CONCLUSIONS

Performance of two horizontal axis wind turbines were analyzed under extreme operating gust and extreme direction change conditions with different initial wind speeds. In the former condition, the magnitude of the wind speed changes while its direction remains fixed, whereas in the latter condition the direction of the wind changes while its speed remains constant. The turbines studied were, the NREL Phase VI turbine and a turbine which was optimized for maximum annual energy production. Both turbines were two-bladed and had a rotor diameter of 10.06m. Performance predictions were performed using CFD and FINE-TURBO package of NUMECA was used for this purpose. Shaft torque, hub bending moment and power coefficient predictions were obtained and presented.

Comparing the performance of the two turbines studied, it was observed that the optimized turbine produced higher torque than NREL Phase VI rotor at lower wind speeds. This was expected because the aerodynamic optimization of this turbine was performed for Gökçeada, Turkey where, the mean wind speed is about 8.8 m/s and most probable wind speed is 6 m/s. However, this higher torque production came at the expense of higher bending loading on the blades compared to NREL Phase VI turbine mainly due to a more severe flow separation observed on the suction side of the optimized blades. As the initial wind speed of the extreme operating gust condition was increased to 10 and 13 m/s, torque production of NREL Phase VI turbine experienced a higher increase during the gust period compared to the optimized turbine. However, bending moment loading on this turbine has also increased faster. A relatively detailed analysis on sectional blade loadings showed that this was mainly due to the airfoil section used at the tip region of the blades. The thinner airfoil profile used at the tip section of the optimized blade slowed the increase of the bending moment. Further increase of the wind speed to 15 m/s led to a highly irregular variation in torque and bending moment produced by the NREL Phase VI rotor. However, these variations remained smooth for the optimized rotor. A closer

look at the sectional flow characteristics of both turbines revealed a periodic vortex shedding in the wake of the NREL Phase VI blades while the wake of the optimized rotor was observed to change slowly in time. This explained the sharp changes in the loading of the NREL Phase VI rotor. Torque and bending moment predictions for 20 m/s initial speed yielded a similar behavior to that was observed for 15m/s.

In the extreme direction change condition, torque and bending moment predictions showed a considerable decline with increasing yaw angle at low wind speeds. The amount of decline decreased as wind speed increased, however, one also has to note that the final yaw angle decreased with increasing wind speed. At higher wind speeds, on the other hand, the final torque output was higher than its initial value even though the yaw error decreases the magnitude of the wind speed component normal to the rotor disk, and hence the power available in the wind. This was mainly because the lower normal wind speed component led to a decrease in the angle of attack of the blade sections and this prevented or delayed flow separation on the suction sides of the blades.

The following conclusions can be drawn when the results are reviewed:

- At low wind speeds, variations in wind speed leads to similar variations in blade loadings. However, this similarity degrades as the wind speed increases.
- Aerodynamic forces do not develop as fast as the wind speed changes; therefore, the instantaneous power coefficient of a rotor may temporarily exceed the Betz limit as the wind speed decreases.
- Using different airfoil sections at different parts of a blade may significantly affect its load variations at unsteady wind conditions.
- Compared to wind speed changes, aerodynamic forces adapt more slowly to wind direction changes.
- Although increasing yaw angle decreases the power available in the wind, at high wind speeds shaft torque produced by the rotor may increase with increasing yaw angle. This due to the fact that the effective angle

of attack of the blades decrease with increasing yaw angle and the flow which is initially separated may eventually become attached.

REFERENCES

- [1] Burton, T., Sharpe, D., Jenkins, N. and Bossanyi, E., 2001. *Wind Energy Handbook, Chapter 3*, John Wiley & Sons, Ltd.
- [2] Hansen, M. O. L., 2008. *Aerodynamics of Wind Turbines*, Earthscan, ISBN: 978-1-84407-438-9.
- [3] Ceyhan, O., 2008. *Aerodynamic Design and Optimization of Horizontal Axis Wind Turbines by using BEM Theory and Genetic Algorithm*, MS Thesis, Middle East Technical University, Ankara, Turkey.
- [4] Sagol, E., 2010. *Site Specific Design Optimization of a Horizontal Axis Wind Turbine based on Minimum Cost of Energy*, MS Thesis, Middle East Technical University, Ankara, Turkey.
- [5] Alpman, E., Kimilli, M. O., Erisik, A., and Sahin, E. 2014. Site-Specific Optimization of a Small Scale Horizontal Axis Wind Turbine via Micro Genetic Algorithm. *Isi Bilimi ve Tekniği Dergisi - Journal of Thermal Science and Technology*, 34 (1), pp. 123 – 136.
- [6] Alpman, E., 2014. Effect of Selection of Design Parameters on the Optimization of a Horizontal Axis Wind Turbine via Genetic Algorithm. *Journal of Physics: Conference Series*, 524, 012044.
- [7] Giguere, P., Selig, M.S., 1999. Design of a Tapered and Twisted Blade for the NREL Combined Experiment Rotor, NREL/SR-500-26173.
- [8] Eke, G. B., Onyewuidala, J. I., 2010. Optimization of Wind Turbine Blades using Genetic Algorithm, *Global Journal of Researches in Engineering*, 10, pp. 22 – 26.
- [9] Diaz-Casas, V., Becerra, J.-A., Lopez-Pena, F., Duro, R. J., 2012. Wind Turbine Design through Evolutionary Algorithms Based on Surrogate CFD Methods, *Optimization Engineering*, DOI 10.1007/s11081-012-9187-1.
- [10] Leishman, J. G., 2002. Challenges in Modelling the Unsteady Aerodynamics of Wind Turbines, *Wind Energy*, 5, pp. 85 – 132.
- [11] Lubitz, W. D., 2014. Impact of Ambient Turbulence on Performance of a Small Wind Turbine, *Renewable Energy*, 61, pp. 69 – 73.
- [12] International Standard IEC 61400-1. Wind Turbines part 1: Design Requirements, 2005.
- [13] Storey, R. C., Norris, S. E., Cater, J.E., 2014. Modelling Turbine Loads during an Extreme Coherent Gust using Large Eddy Simulation, *Journal of Physics: Conference Series*, 524, 012177.
- [14] Storey, R. C., Norris, S. E., Cater, J.E., 2014. An Actuator Sector Method for Efficient Wind Turbine Simulation, *Wind Energy*, DOI: 10.1002/we.1722.
- [15] Jeong, M.-S., Kim, S.-W. Lee, I., Yoo, S.-J., 2014. Wake Impacts on Aerodynamic and Aeroelastic Behaviors of a Horizontal Axis Wind Turbine Blade for Sheared Turbulent Flow, *Journal of Fluids and Structures*, 50, pp. 66 – 78.
- [16] Kim, T., Petersen, M. M., Larsen, T. J., 2014. A Comparison Study of the Two-Bladed Partial Pitch Turbine During Normal Operation and Extreme Gust Conditions, *Journal of Physics: Conference Series*, 524, 012065.
- [17] <http://www.hawc2.dk/>
- [18] Qui, Y.-X. Wang, X.-D., Kang, S., Zhao, M., Liang, Y.-J., 2014. Predictions of Unsteady HAWT Aerodynamics in Yawing and Pitching using Free-Vortex Method, *Renewable Energy*, 70, pp. 93 – 106.
- [19] Sezer-Uzol, N., Uzol, O., 2013. Effect of Steady and Transient Wind Shear on the Wake Structure and Performance of a Horizontal Axis Wind Turbine Rotor, *Wind Energy*, 16, pp. 1-17.
- [20] Jeon, M., Lee, S., Lee, S., 2014. Unsteady Aerodynamics of Off-Shore Floating Wind Turbines in Platform Pitching Motion using Vortex Lattice Method, *Renewable Energy*, 65, pp. 207 – 212.
- [21] Wekesa, D. W., Wang, C., Wei, Y., Danao, L. A. M., 2014. Influence of Operating Conditions on Unsteady Wind Performance of Vertical Axis Wind Turbines Operating within a Fluctuating Free-Stream: A Numerical Study, *Journal of Wind Engineering and Industrial Aerodynamics*, 135, pp. 76 – 89.
- [22] Wekesa, D. W., Wang, C., Wei, Y., Kamau, J. N., Danao, L. A. M., 2015. A Numerical Analysis of Unsteady Wind Site for Site Specific Vertical Axis Wind Turbine: A Case Study for Marsabit and Garissa in Kenya, *Renewable Energy*, 76, pp. 648 – 661.
- [23] <http://www.numeca.com/index.php?id=turbomachine>
- [24] Spalart, P. R. and Allmaras, S. R., 1992. A One-Equation Turbulence Model for Aerodynamic Flows, *AIAA Paper*, 92-0439.
- [25] Sorensen, N. N., Michelsen, J. A. and Schreck, S., 2002. Navier-Stokes Predictions of the NREL Phase VI Rotor in the NASA Ames 80ft x 120ft Wind Tunnel, *Wind Energy*, 5, pp. 151 – 169.
- [26] FINE™/Turbo v8.7 User Manual, Numeca International, 2010.
- [27] Simms, D., Schreck, S., Hand, M. and Fingersh, L. J., 2001. NREL Unsteady Aerodynamics Experiment in the NASA-Ames Wind Tunnel: A Comparison of Predictions to Measurements. *NREL/TP-500-29494*.
- [28] Somers, D. M., 1997. Design and Experimental Results for the S809 Airfoil, *NREL/SR-440-6918*.
- [29] Williamson, G. A., McGranahan, B. D., Broughton, B. A., Deters, R. W., Brandt, J. B., Selig, M. S., 2012. Summary of Low-Speed Airfoil Data: Volume 5, *University of Illinois Low Speed Airfoil Tests*.
- [30] <https://wind.nrel.gov/airfoils/AirfoilList.html>
- [31] Selig, M. S., McGranahan, B. D., 2004. Wind Tunnel Tests of Six Airfoils for Use on Small Wind Turbines, *NREL/SR-500-34515*.